LETTER

https://doi.org/10.1038/s41586-018-0061-y

Structure of the alternative complex III in a supercomplex with cytochrome oxidase

Chang Sun[1,2,9], Samir Benlekbir[3,9], Padmaja Venkatakrishnan[1,8,9], Yuhang Wang[1,2,4], Sangjin Hong[1], Jonathan Hosler[5], Emad Tajkhorshid[1,2,4,10]*, John L. Rubinstein[3,6,7,10]* & Robert B. Gennis[1,10]*

Alternative complex III (ACIII) is a key component of the respiratory and/or photosynthetic electron transport chains of many bacteria[1–3]. Like complex III (also known as the bc_1 complex), ACIII catalyses the oxidation of membrane-bound quinol and the reduction of cytochrome *c* or an equivalent electron carrier. However, the two complexes have no structural similarity[4–7]. Although ACIII has eluded structural characterization, several of its subunits are known to be homologous to members of the complex iron–sulfur molybdoenzyme (CISM) superfamily[8], including the proton pump polysulfide reductase[9,10]. We isolated the ACIII from *Flavobacterium johnsoniae* with native lipids using styrene maleic acid copolymer[11–14], both as an independent enzyme and as a functional 1:1 supercomplex with an aa_3-type cytochrome *c* oxidase (cyt aa_3). We determined the structure of ACIII to 3.4 Å resolution by cryo-electron microscopy and constructed an atomic model for its six subunits. The structure, which contains a [3Fe–4S] cluster, a [4Fe–4S] cluster and six haem *c* units, shows that ACIII uses known elements from other electron transport complexes arranged in a previously unknown manner. Modelling of the cyt aa_3 component of the supercomplex revealed that it is structurally modified to facilitate association with ACIII, illustrating the importance of the supercomplex in this electron transport chain. The structure also resolves two of the subunits of ACIII that are anchored to the lipid bilayer with N-terminal triacylated cysteine residues, an important post-translational modification found in numerous prokaryotic membrane proteins that has not previously been observed structurally in a lipid bilayer.

The ACIII–cyt aa_3 supercomplex from *F. johnsoniae* membranes was solubilized, purified and biochemically characterized using styrene maleic acid (SMA) copolymer nanodiscs without traditional detergents (Supplementary Discussion, Extended Data Figs. 1–3). The supercomplex catalyses the two-electron oxidation of menaquinol (or ubiquinol) and the four-electron reduction of oxygen to water with a turnover number of around 21 electrons per second without the addition of exogenous cyt *c* (Supplementary Information, Extended Data Fig. 3), indicating a functional electron transfer chain within the supercomplex. The addition of exogeneous cyt *c* did not increase the rate of electron transfer. The structure of the ACIII–cyt aa_3 supercomplex in SMA nanodiscs was determined by cryo-electron microscopy (cryo-EM) (Fig. 1, Extended Data Fig. 4). The supercomplex has a mass of 464 kDa (Supplementary Discussion), a transmembrane cross-section of approximately 9 nm × 13 nm (Extended Data Fig. 5), and contains 48 transmembrane α-helices. To our knowledge, the ACIII–cyt aa_3 supercomplex is the largest protein complex reported to be contained within an SMA copolymer nanodisc. The SMA copolymer and lipids contribute only a thin layer of density around the supercomplex (Fig. 1a, b), which is not circular but follows the contours of the protein. Whether this is a general feature of SMA-solubilized proteins or is due to the large size of the ACIII–cyt aa_3 supercomplex is not known, and will be clarified when more structures are determined using this approach. The number of loosely bound, unresolved lipid molecules is not known, nor is it known whether they are sufficient in number to form a true bilayer surrounding the protein. The SMA–supercomplex nanodiscs retain native lipids, are more stable and have 30% higher specific activity than the supercomplex isolated with detergents (for example, dodecylmaltoside) (Supplementary Discussion, Extended Data Fig. 3). Because traditional detergents are avoided in generating SMA nanodiscs, the preparative protocol is more rapid and simpler than making nanodiscs using membrane scaffold proteins.

Although the properties of the SMA nanodiscs are less well characterized than nanodiscs made with membrane scaffold proteins[13,15], our work demonstrates the utility of SMA nanodiscs for high-resolution structural studies of membrane proteins.

The resolution of the cryo-EM density map enabled construction of an atomic model for more than 90% of the sequences predicted from the ACIII gene cluster (Supplementary Discussion), including subunits ActA, ActB, ActC, ActD, ActE and ActF (Fig. 2, Extended Data Fig. 5, Extended Data Table 1). Sequence analysis shows that ACIII contains a unique combination of known modules from other respiratory complexes[3] (Supplementary Discussion). The ACIII structure confirms this prediction and shows the structure responsible for catalysing the quinol:cyt *c* oxidoreductase activity. The ACIII structure can be divided into three parts: a core assembly of ActC and ActB that oxidizes quinol; a haem *c* assembly consisting of ActA and ActE that directs electrons from ActB to the terminal electron acceptor; and auxiliary transmembrane subunits ActD and ActF with unknown functions. With some key differences (Extended Data Fig. 5), the overall architecture of ActB and ActC resembles the complex consisting of the PsrA, PsrB and PsrC

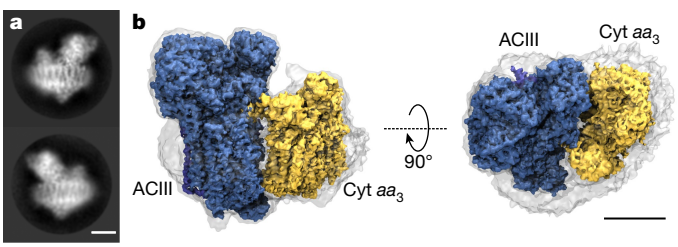

Fig. 1 | Cryo-EM of the ACIII–cyt aa_3 supercomplex in SMA nanodiscs. **a**, Two representative 2D class average images of the ACIII–cyt aa_3 supercomplex in a nanodisc. Calculation of 2D class averages was not repeated. **b**, Side (left) and top (right) views of the ACIII–cyt aa_3 supercomplex cryo-EM map. The transparent surface indicates the boundary of the nanodisc. Scale bars, 50 Å.

[1]Department of Biochemistry, University of Illinois, Urbana, IL, USA. [2]NIH Center for Macromolecular Modeling and Bioinformatics, Beckman Institute for Advanced Science and Technology, University of Illinois, Urbana, IL, USA. [3]Molecular Medicine Program, The Hospital for Sick Children Research Institute, Toronto, Ontario, Canada. [4]Center for Biophysics and Quantitative Biology, University of Illinois, Urbana, IL, USA. [5]Department of Biochemistry, University of Mississippi Medical Center, Jackson, MS, USA. [6]Department of Medical Biophysics, The University of Toronto, Toronto, Ontario, Canada. [7]Department of Biochemistry, The University of Toronto, Toronto, Ontario, Canada. [8]Present address: Department of Microbiology and Molecular Genetics, University of California, Davis, Davis, CA, USA. [9]These authors contributed equally: C. Sun, S. Benlekbir, P. Venkatakrishnan. [10]These authors jointly supervised this work: E. Tajkhorshid, J. L. Rubinstein, R. B. Gennis. *e-mail: emad@life.illinois.edu; john.rubinstein@utoronto.ca; r-gennis@illinois.edu

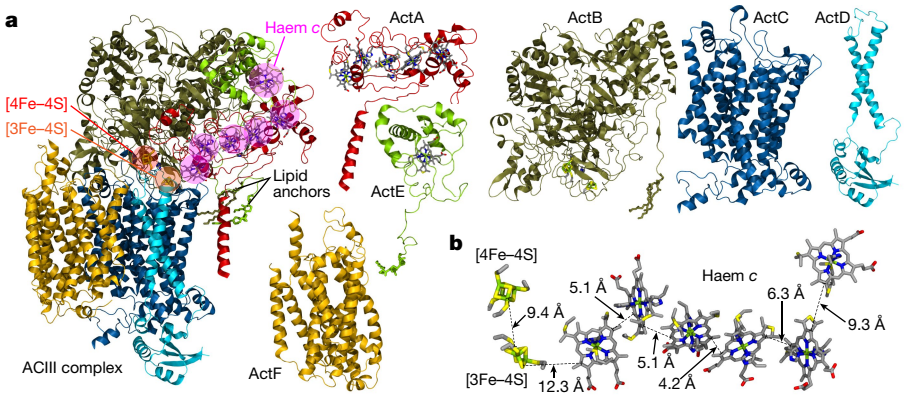

Fig. 2 | Atomic model of ACIII. a, The overall structure is shown on the left, along with separate views of individual subunits. Covalently bonded cysteines are shown along with the core iron–sulfur clusters (circled in orange). Both covalently linked cysteines and axial-coordinating residues are shown for haems (circled in pink). **b**, The edge-to-edge distances between cofactors.

subunits of polysulfide reductase from *Thermus thermophilus* (PsrABC)[16], a member of the CISM superfamily (Supplementary Discussion). Like PsrC, ActC contains no cofactors, but it does contain the proposed site for the oxidation of menaquinol. Residues at the menaquinol-binding site identified in PsrC[16] are not conserved in ActC[17]. Although menaquinone is not observed in the cryo-EM map, we propose that the ActC residues His133 and Asp164 form the menaquinol-binding site in ActC near the interface with ActB (Extended Data Fig. 6). These two residues are conserved in ActC sequences and there is a crevice between transmembrane helices 3 (TM3) and 4 (TM4) of ActC that would provide access to the substrate in the membrane bilayer.

The N-terminal portion of ActB is homologous to the PsrA subunit of polysulfide reductase, which contains the molybdenum cofactor, but the molybdenum cofactor is absent in ActB[4]. The C-terminal domain of ActB is homologous to PsrB, and both ActB and PsrB contain iron–sulfur clusters. Like PsrB, ActB from *F. johnsoniae* is expected to contain four iron–sulfur clusters, but only two are observed in the cryo-EM map (Extended Data Fig. 7). There is one [3Fe–4S] cluster near the interface with ActC, about 10 Å from the proposed site of menaquinol oxidation, and one [4Fe–4S] cluster about 9 Å further away. There are two additional cysteine clusters present in the structure of ActB, but the cryo-EM map does not show iron–sulfur clusters at these locations. Instead, we observe disulfide bonds (Cys965–Cys938 and Cys971–Cys769) within these two cysteine clusters in ActB. The substitution of proposed [4Fe–4S] clusters by disulfide bonds may be a genuine aspect of the structure or may result from oxidation that occurred during sample preparation. However, if these two 'missing' [4Fe–4S] clusters were present, they would form a dead-end for electron transfer from the [3Fe–4S] cluster of ActB, suggesting that their absence from the structure is not an artefact.

The [3Fe–4S] cluster in ActB is the most probable initial oxidant of menaquinol bound to ActC, and is 12.3 Å from the nearest haem *c* in ActA. The five haems *c* in ActA plus the single haem *c* in ActE form a probable electron transfer wire from the [3Fe–4S] cluster in ActB, with the largest edge-to-edge distance of 9.2 Å between adjacent haems (Fig. 2b). The [4Fe–4S] cluster in ActB appears to be off-pathway and its function remains to be determined.

In all *Flavobacteria*, including *F. johnsoniae*, ActA is predicted to have a monohaem domain at the N terminus in addition to the pentahaem domain at the C terminus (Supplementary Discussion). Mass spectrometry analysis shows that the N-terminal monohaem domain is present in the preparation (Extended Data Fig. 1), but no density can be assigned to this entire domain. The inability to resolve the monohaem domain may result from flexibility of the domain. Full-atom molecular dynamics simulations were performed for the entire structure of ACIII embedded in a phospholipid bilayer to determine the stability and dynamics of the structure (Extended Data Fig. 8). Notably, the pentahaem domain of ActA had the largest root-mean-square deviation (r.m.s.d.), which arises mainly from the transmembrane α-helix connected to the missing monohaem domain; this is consistent with the monohaem domain being unobservable owing to a variable position in the complex. Although ActE also had a substantial r.m.s.d., it did not appear to correlate with disorder in the cryo-EM map.

ActD and ActF are transmembrane subunits without bound cofactors, and both interact with ActC. It has not been established whether ACIII generates a proton motive force coupled to electron transport[18]. The absence of redox centres in ActC, ActD and ActF suggests that if ACIII contributes to the transmembrane proton gradient, it does not use the bifurcation-type Q-cycle mechanism of canonical complex III[19], but instead functions as a true proton pump with a mechanism that resembles that of complex I[20]. ActD has two transmembrane α-helices that cross within the membrane and are adjacent to ActC. Both N and C termini are within the cytoplasm and combine to form a single globular domain that rests on the cytoplasmic surface of ActC. The ten transmembrane α-helices of ActF form a pseudo two-fold axis of symmetry with the ten transmembrane α-helices of ActC (Extended Data Fig. 5), despite the fact that ActF has less than 20% sequence identity with ActC. If ACIII is a proton pump, it is likely that conserved polar residues within the bilayer will have important roles.

The structure of ACIII reveals eleven ordered phospholipid molecules as well as triacylated cysteine residues at the N termini of ActB (Fig. 3a) and ActE (Extended Data Fig. 7). The anchoring of bacterial membrane proteins by an N-terminal triacylated cysteine is a well-characterized phenomenon[21]; however, to our knowledge, this is the first time the structure of a triacylated cysteine residue has been determined in the context of a membrane protein. Both lipid anchors are tilted with respect to the plane of the lipid bilayer (Fig. 2a), restricting the ability of other lipids to pack around them. This feature could alter the mechanical properties of the adjacent portion of the membrane bilayer, and also guide conformational changes in the ACIII protein. Notably, the two N-terminal lipid anchors are adjacent to each other in the membrane. These lipid anchors probably help ACIII to assemble and keep the monohaem ActE bound to the complex. The eleven lipids that are resolved adjacent to the transmembrane α-helices accommodate the rugged protein surface of the complex (Fig. 3b, Extended Data Fig. 7). The head groups of the lipids could not be identified and were all modelled as phosphatidylethanolamine. There are two 'hot spots' for resolved lipids: the cytoplasmic interface between ActC and ActF; and the vicinity of the triacylated cysteine of ActB, which is near the proposed entry point for menaquinol into the complex. All eleven of the resolved lipids remained bound to the protein throughout 250 ns of molecular dynamics simulation (Extended Data Fig. 8), supporting the ability of SMA nanodiscs to preserve some native lipid–protein interactions and suggesting a functional role for the lipids. A large number of annular lipids, including those modelled in the structure, were observed to associate with the protein from the in silico bilayer.

Frequently, the subunits encoding ACIII are within an operon that includes subunits of an associated complex IV[3] (cyt aa_3 or cyt caa_3). We find that the sequences of subunit III from complex IVs that are associated with ACIII have unusual features that distinguish them from the canonical subunit III (Supplementary Discussion).

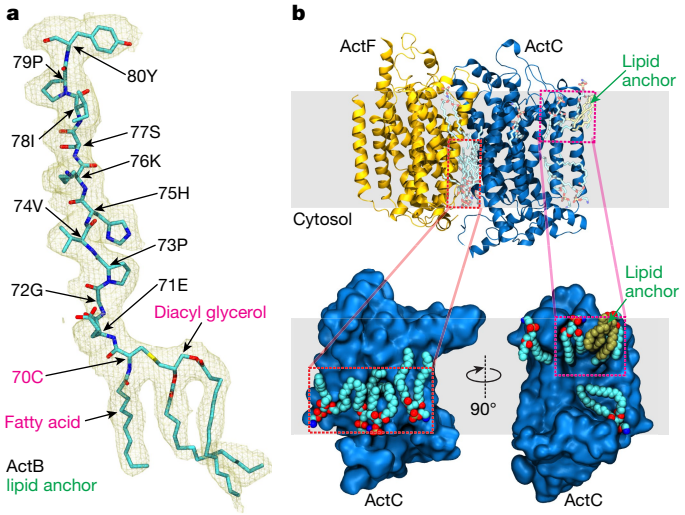

Fig. 3 | Lipids in the structure of ACIII. a, Triacylated cysteine at the N terminus of ActB. The triacylated cysteine and its downstream ten amino acid residues are shown in the context of the experimental density map. **b**, Other resolved lipids near the transmembrane α-helices. Four lipid molecules are resolved at the cytoplasmic interface between ActC and ActF. Alongside, two lipid molecules are clustered near the triacylated cysteine from ActB, directly above the proposed quinone entry pathway.

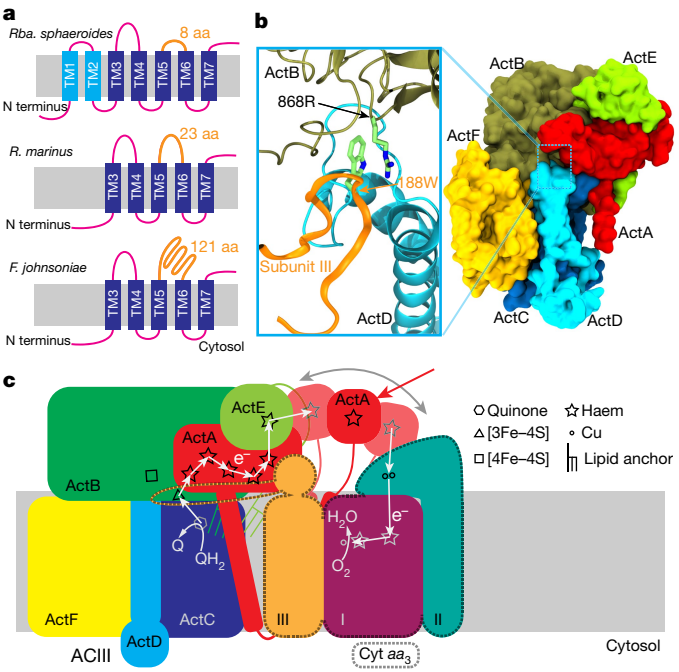

Fig. 4 | ACIII–cyt *aa*$_3$ supercomplex in *F. johnsoniae*. a, Topology comparison of subunit III of cyt *aa*$_3$ from different species. **b**, Tryptophan 188 from the subunit III loop (orange) of cyt *aa*$_3$ interacts with arginine 868 from the subunit B of ACIII. The surface representation of ACIII on the right shows the binding pocket for the subunit III loop. **c**, Working model for electron transfer in the ACIII–cyt *aa*$_3$ supercomplex.

Whereas subunit III of complex IV generally contains seven transmembrane α-helices, those that are associated with ACIII lack TM1 and TM2 (Fig. 4a). Although only parts of subunit III of cyt *aa*$_3$ are resolved to better than 4 Å, the density for cyt *aa*$_3$ has sufficient resolution to identify five α-helices from the structure. A homology model of subunit III from *F. johnsoniae* cyt *aa*$_3$ was built on the basis of the structure of TM3 to TM7 of subunit III from *Rhodobacter sphaeroides* cyt *aa*$_3$, and fit into the ACIII–cyt *aa*$_3$ supercomplex density map (Extended Data Fig. 9) with high fidelity. The deletion of the first two transmembrane α-helices in subunit III of cyt *aa*$_3$ appears to be a necessary adaptation to enable formation of the supercomplex with ACIII. It is notable that the same two helices in subunit III are also absent in the cyt *aa*$_3$ obligatory cyt *bcc*–cyt *aa*$_3$ supercomplex found in *Actinobacteria* (for example, *Corynebacterium glutamicum* and *Mycobacterium tuberculosis*)[22].

The sequence analysis also reveals that the loop between TM5 and TM6 of subunit III in the cyt *aa*$_3$ that is part of the supercomplex is much longer in *F. johnsoniae* (and all *Flavobacteria*) than in other organisms. Typically, this loop contains eight residues, but in *F. johnsoniae* it contains 121 residues (Fig. 4a). Part of this long loop fits in a groove between ActB and ActD of ACIII on the periplasmic side of the membrane (Extended Data Fig. 9). The structural model reveals a π–cation interaction between Trp188 of subunit III and Arg868 of ActB (Fig. 4b), both of which are conserved among organisms containing subunit III with a long loop between TM5 and TM6 (Extended Data Fig. 9). This specific and strong interaction stabilizes the ACIII–cyt *aa*$_3$ supercomplex and appears to be a second adaptation that enables the formation of a supercomplex with ACIII. The contact between the periplasmic loop of subunit III of cyt *aa*$_3$ and ACIII is the only observed direct contact between the two complexes. The five well-resolved transmembrane α-helices of subunit III of cyt *aa*$_3$ are angled away from ACIII with only the tip of TM6 of subunit III touching ActF, forming a wedge-like space between the membrane domains of ACIII and cyt *aa*$_3$. The decrease of resolution in the portions of cyt *aa*$_3$ that are distant from the interface with ACIII suggests that there may be several conformations of the supercomplex that are all tethered by the loop in cyt *aa*$_3$. The loop could, therefore, serve as a hinge, enabling the membrane domains of ACIII and cyt *aa*$_3$ to swing into contact transiently.

Using the location of TM3 to TM7 of subunit III within the supercomplex as a guide enables a model of the entire cyt *aa*$_3$ to be placed within the density map for the supercomplex (Extended Data Fig. 9).

In the resulting model, there is a considerable distance (56 Å) between the haem *c* in ActE of ACIII and Cu_A within subunit II of cyt *aa*$_3$. Electron transfer within the supercomplex does not require the addition of exogenous cyt *c*, which is also the case for the cyt *bcc*-cyt *aa*$_3$ supercomplex from *C. glutamicum*[23]. It is possible, although it seems unlikely, that there is a subset of conformations in which ActE comes close enough to cyt *aa*$_3$ for direct electron transfer. It is noteworthy that the monohaem domain of ActA has substantial sequence homology (around 30% identity) with the haem *c* domain that is present at the C terminus of subunit II of cyt *caa*$_3$ from *T. thermophilus*. This observation suggests that the ActA monohaem domain, which we postulate to be highly mobile in the structure (see above), may be able to interact with subunit II of cyt *aa*$_3$ and shuttle electrons from the ActE monohaem domain to subunit II of cyt *aa*$_3$. As such, electron transfer within the supercomplex may require the monohaem domain of ACIII to swing back and forth between ACIII and cyt *aa*$_3$ to shuttle electrons (Fig. 4c). Additional experimental work will be required to test this model and, indeed, to determine the physiological advantage of forming the supercomplex.

We would like to note that, contemporaneously with our studies, Sousa et al.[24] determined the structure of the homologous ACIII from *Rhodothermus marinus* by cryo-EM at 3.9 Å resolution. Aside from species-specific variations, the reported structures of the ACIIIs of *F. johnsoniae* and *R. marinus* are compatible. The observation made here that, like canonical complexes III and IV, ACIII and an adapted complex IV can also form a supercomplex hints at the importance of supercomplexes in oxidative phosphorylation. We demonstrate that high-resolution cryo-EM with SMA nanodiscs, which preserves native protein–protein and protein–lipid interactions, is ideally suited to have an important role in future studies.

Online content

Any Methods, including any statements of data availability and Nature Research reporting summaries, along with any additional references and Source Data files, are available in the online version of the paper at https://doi.org/10.1038/s41586-018-0061-y.

Received: 26 November 2017; Accepted: 20 March 2018;
Published online 25 April 2018.

1. Pereira, M. M., Carita, J. N. & Teixeira, M. Membrane-bound electron transfer chain of the thermohalophilic bacterium *Rhodothermus marinus*: a novel multihemic cytochrome *bc*, a new complex III. *Biochemistry* **38**, 1268–1275 (1999).
2. Yanyushin, M. F., del Rosario, M. C., Brune, D. C. & Blankenship, R. E. New class of bacterial membrane oxidoreductases. *Biochemistry* **44**, 10037–10045 (2005).
3. Refojo, P. N., Sousa, F. L., Teixeira, M. & Pereira, M. M. The alternative complex III: a different architecture using known building modules. *Biochim. Biophys. Acta* **1797**, 1869–1876 (2010).
4. Pereira, M. M., Refojo, P. N., Hreggvidsson, G. O., Hjorleifsdottir, S. & Teixeira, M. The alternative complex III from *Rhodothermus marinus* - a prototype of a new family of quinol:electron acceptor oxidoreductases. *FEBS Lett.* **581**, 4831–4835 (2007).
5. Gao, X., Xin, Y., Bell, P. D., Wen, J. & Blankenship, R. E. Structural analysis of alternative complex III in the photosynthetic electron transfer chain of *Chloroflexus aurantiacus*. *Biochemistry* **49**, 6670–6679 (2010).
6. Refojo, P. N., Ribeiro, M. A., Calisto, F., Teixeira, M. & Pereira, M. M. Structural composition of alternative complex III: variations on the same theme. *Biochim. Biophys. Acta* **1827**, 1378–1382 (2013).
7. Xia, D. et al. Crystal structure of the cytochrome bc_1 complex from bovine heart mitochondria. *Science* **277**, 60–66 (1997).
8. Rothery, R. A., Workun, G. J. & Weiner, J. H. The prokaryotic complex iron–sulfur molybdoenzyme family. *Biochim. Biophys. Acta* **1778**, 1897–1929 (2008).
9. Dietrich, W. & Klimmek, O. The function of methyl-menaquinone-6 and polysulfide reductase membrane anchor (PsrC) in polysulfide respiration of *Wolinella succinogenes*. *Eur. J. Biochem.* **269**, 1086–1095 (2002).
10. Hedderich, R. et al. Anaerobic respiration with elemental sulfur and with disulfides. *FEMS Microbiol. Rev.* **22**, 353–381 (1998).
11. Dörr, J. M. et al. Detergent-free isolation, characterization, and functional reconstitution of a tetrameric K^+ channel: the power of native nanodiscs. *Proc. Natl Acad. Sci. USA* **111**, 18607–18612 (2014).
12. Postis, V. et al. The use of SMALPs as a novel membrane protein scaffold for structure study by negative stain electron microscopy. *Biochim. Biophys. Acta* **1848**, 496–501 (2015).
13. Dörr, J. M. et al. The styrene–maleic acid copolymer: a versatile tool in membrane research. *Eur. Biophys. J.* **45**, 3–21 (2016).
14. Parmar, M. et al. Using a SMALP platform to determine a sub-nm single particle cryo-EM membrane protein structure. *Biochim. Biophys. Acta* **1860**, 378–383 (2018).
15. Bayburt, T. H. & Sligar, S. G. Membrane protein assembly into nanodiscs. *FEBS Lett.* **584**, 1721–1727 (2010).
16. Jormakka, M. et al. Molecular mechanism of energy conservation in polysulfide respiration. *Nat. Struct. Mol. Biol.* **15**, 730–737 (2008).
17. Majumder, E. L., King, J. D. & Blankenship, R. E. Alternative complex III from phototrophic bacteria and its electron acceptor auracyanin. *Biochim. Biophys. Acta* **1827**, 1383–1391 (2013).
18. Refojo, P. N., Teixeira, M. & Pereira, M. M. The alternative complex III: properties and possible mechanisms for electron transfer and energy conservation. *Biochim. Biophys. Acta* **1817**, 1852–1859 (2012).
19. Crofts, A. R. The cytochrome bc_1 complex: function in the context of structure. *Annu. Rev. Physiol.* **66**, 689–733 (2004).
20. Sazanov, L. A. A giant molecular proton pump: structure and mechanism of respiratory complex I. *Nat. Rev. Mol. Cell Biol.* **16**, 375–388 (2015).
21. Kovacs-Simon, A., Titball, R. W. & Michell, S. L. Lipoproteins of bacterial pathogens. *Infect. Immun.* **79**, 548–561 (2011).
22. Kao, W. C. et al. The obligate respiratory supercomplex from *Actinobacteria*. *Biochim. Biophys. Acta* **1857**, 1705–1714 (2016).
23. Graf, S. et al. Rapid electron transfer within the III–IV supercomplex in *Corynebacterium glutamicum*. *Sci. Rep.* **6**, 34098 (2016).
24. Sousa, J. S. et al. Structural basis for energy transduction by respiratory alternative complex III. *Nat. Commun*. (in the press).

Acknowledgements This work was supported by funds from the National Institutes of Health (R01-HL016101 to R.B.G.; P41-GM104601, U54-GM087519 and R01-GM123455 to E.T.) and Canadian Institutes of Health Research (MOP-81294 to J.L.R.); J.L.R. was supported by the Canada Research Chairs program. Some of this work was performed at the Simons Electron Microscopy Center and National Resource for Automated Molecular Microscopy, supported by grants from the Simons Foundation (349247), and the National Institute of General Medical Sciences (P41-GM103310, S10-OD019994). Molecular dynamics simulations were performed at Blue Waters (ACI-1713784 to E.T.) and XSEDE (TG-MCA06N060 to E.T.). Blue Waters is supported by the National Science Foundation (OCI-0725070 and ACI-1238993) and the State of Illinois. XSEDE is supported by the National Science Foundation (ACI-1548562). We thank M. McBride for providing us with the *Flavobacterium johnsoniae* UW101 strain, B. Carragher and C. Potter for facilitating access to the Titan Krios, Z. Zhang for collecting data, and M. Mazhab-Jafari for advice on building atomic models.

Reviewer information *Nature* thanks Y. Cheng, M. Wikström and the other anonymous reviewer(s) for their contribution to the peer review of this work.

Author contributions P.V. expressed, purified and characterized the protein supercomplex, S.B. prepared cryo-EM specimens and calculated cryo-EM maps, C.S. built the de novo atomic structures, Y.W. conducted the molecular dynamics simulations, S.H. performed the electrochemical characterization, J.H. performed the metal analysis, E.T. supervised molecular dynamics simulations, J.L.R. supervised the molecular structure determination, and R.B.G. conceived the project, supervised biochemical experiments, and coordinated the project. All authors participated in the manuscript preparation.

Competing interests The authors declare no competing interests.

Additional information
Extended data is available for this paper at https://doi.org/10.1038/s41586-018-0061-y.
Supplementary information is available for this paper at https://doi.org/10.1038/s41586-018-0061-y.
Reprints and permissions information is available at http://www.nature.com/reprints.
Correspondence and requests for materials should be addressed to E.T., J.L.R. or R.B.G.
Publisher's note: Springer Nature remains neutral with regard to jurisdictional claims in published maps and institutional affiliations.

METHODS

Bacterial strain and growth conditions. *Flavobacterium johnsoniae* ATCC 17061 strain UW101 was used in this study. The strain was a gift from M. McBride at the University of Wisconsin, Milwaukee. The cells were grown in casitone-yeast extract medium at 30 °C under high aerobic conditions (500 ml cultures in 2 l flasks)[25].

Membrane preparation and protein purification. Cells grown overnight were collected by centrifugation (14,000*g* for 10 min). The cell pellet from 12 l of culture (~2.5 g l^{-1}) was resuspended in ~200 ml of 20 mM Tris-HCl buffer, pH 8 (buffer A) with 5 mM $MgSO_4$, DNase I (Sigma) and a protease inhibitor cocktail (Sigma). This suspension was passed three times through a Microfluidizer at a pressure of 80,000 psi to disrupt the cells. The cell extract was centrifuged at 14,000*g* for 10 min to remove unbroken cells. Membranes were obtained after centrifugation at 185,500*g* for 4 h. Under the above growth conditions, the membranes contained ACIII, cyt aa_3 and cyt *bd*. The membrane pellet was solubilized by using either a traditional detergent or the SMA copolymer.

Purification using Triton X-100 and DDM. The membrane pellet was resuspended in buffer A (~50 mg ml^{-1}) along with 300 mM NaCl, and solubilized by the addition of Triton X-100 (Fisher Scientific) to a final concentration of 4%. The solution was incubated at 4 °C for 2 h with mild agitation. The suspension was cleared by centrifugation at 185,500*g* for 1 h, after which the detergent was diluted fourfold by adding three volumes of buffer A to the supernatant. The diluted supernatant was then added to a chromatography column containing 10 ml of Ni–NTA resin (Qiagen) pre-equilibrated with 20 mM Tris-HCl pH 8 containing 0.05% Triton X-100 and 0.15 M NaCl (buffer B). The resin was washed with about ten column volumes of buffer B to remove any unbound sample. Detergent exchange to *n*-dodecyl-β-D-maltoside (DDM; Anatrace) was carried out by washing with buffer B containing 0.05% DDM instead of Triton X-100 (buffer C). The column was further washed with five column volumes of buffer C containing 10 mM imidazole to remove the loosely bound proteins from the resin. The proteins that were well bound to the resin were eluted using 100 mM imidazole in buffer C. The eluent was concentrated to around 3 ml using Amicon Ultra-15 filters (Millipore) with a 100-kDa cutoff. The excess imidazole was removed by dialysis against buffer C. The yield of protein obtained was about 0.3 mg l^{-1} of ACIII and 0.16 mg l^{-1} of cyt aa_3 from 12 l of culture. When indicated, the proteins were further purified by gel filtration chromatography using a Superdex 200 10/300 GL column (GE Healthcare Life Sciences). The purified proteins were stored at −80 °C after adding glycerol to a final concentration of 10%.

Purification using SMA copolymer. The SMA copolymer SMA 3000HNA (styrene maleic acid copolymer, ~3:1 molar ratio of styrene:maleic acid) was a gift from T. Bricker (Louisiana State University) who used SMA copolymer made by Cray Valley USA (now Total Petrochemicals & Refining USA) successfully for the studies of photosystem from spinach thylakoids[26]. Additional SMA 3000HNA was provided by Total Petrochemicals & Refining USA as an aqueous solution of 25.6% (w/v) SMA. We also used a similar product, Xiran SL25010 S25, provided by Polyscope Polymers B. V., with similar results. These polymer preparations are provided as aqueous solutions of the sodium salt, and the polymer solutions were simply diluted to the final desired percentage to use directly for the solubilization of membranes. The purification protocol with the SMA copolymer was similar to that described with detergents with the following differences. After the membrane pellet was resuspended, the SMA solution was added dropwise to a final concentration of 1% with continuous stirring. After incubation for 1 h at room temperature, the solution was centrifuged at 185,500*g* for 1 h to remove unsolubilized particles. The supernatant was loaded directly to the Ni–NTA column equilibrated with 20 mM Tris-HCl pH 8, 0.15 M NaCl. The remaining steps of the purification were as described above. After solubilization of the membrane suspension with 1% SMA 3000HNA, no additional SMA or detergents were added and were not needed to maintain the solubilized proteins in solution. The yield of protein after the use of the SMA copolymer for solubilization was about 0.5 mg l^{-1} for ACIII and about 0.15 mg l^{-1} for cyt aa_3 from 12 l of culture.

Analytical methods. The total protein concentration was determined using the BCA kit (Thermo Scientific, Pierce Protein Research Products). The UV–visible absorption spectra of the oxidized and reduced proteins were recorded on an Agilent Technologies spectrophotometer (model 8453). The pyridine haemochrome assay[27] was used to determine the concentration of haems present in the protein samples. The total haem *c* concentration was divided by seven to calculate the ACIII concentration and the total haem *a* concentration was divided by two to calculate the cyt aa_3 concentration. The purified protein was analysed by SDS–PAGE using 4–20% precast gels (Nusep Tech). Haem staining was carried out using 3,3′,5,5′-tetramethyl benzidene (TMBZ)[28]. The supercomplex was visualized by blue native PAGE (BN–PAGE) using a 4–16% gel (Novex, Life Technologies) with Bis-Tris buffer. The entire gel was stained with Coomassie blue, and then fixed with 30% methanol and 10% glacial acetic acid. The gel was destained with 8% glacial acetic acid to visualize the bands. Peptide mass spectrometry and analyses were carried out by P. Yau at the Roy J. Carver Biotechnology Center at the University of Illinois at Urbana-Champaign.

Oxygen consumption assay. Oxygen consumption was measured using a Clark electrode (Strathkelvin) in a 1 ml chamber at 25 °C as previously described[29]. The reaction mix consisted of 100 μM ubiquinone-1 (Q_1; Sigma-Aldrich) and 5 mM dithiothreitol in air-saturated 0.1 M potassium phosphate buffer, pH 7.5 with 150 mM NaCl. The reaction was started by adding the purified protein into the chamber. The initial concentration of oxygen was calculated to be 237 μM.

Quinol:cytochrome *c* oxidoreductase activity. The quinol:cytochrome *c* oxidoreductase activity of the ACIII was measured spectrophotometrically as described previously[30]. The reaction was carried out in a 2 ml anaerobic cuvette, at 25 °C in 50 mM potassium phosphate buffer, pH 7.5 in the presence of 50 μM horse heart cytochrome *c* (Sigma-Aldrich) and 200 μM KCN. Ubiquinol-1 (Q_1H_2) or reduced vitamin K_2 (Sigma-Aldrich) were used as quinol substrates and, in each case, the quinone was reduced using sodium borohydride according to a previously described method[31]. The reaction was started by the addition of 100 μM of reduced quinone.

EPR spectroscopy. The purified ACIII–cyt aa_3 supercomplex was extensively dialysed against 20 mM Tris-HCl buffer, pH 8, with 150 mM NaCl and 1 mM EDTA to eliminate adventitious transition metal ions. The sample was concentrated in an Amicon filter to 150 μl with a final ACIII concentration of around 60 μM. The air-oxidized sample was directly transferred to an X-band EPR tube and subsequently frozen in liquid nitrogen. The sample was oxidized completely by the addition of 2 mM potassium ferricyanide. Glycerol (5%) was present in all EPR samples. Continuous wave EPR measurements were carried out on an X-band Varian EPR-E122 spectrometer at the Electron Paramagnetic Resonance facility at the University of Illinois at Urbana-Champaign. Cryogenic conditions below 77 K were achieved with a Lakeshore 331 temperature controller using a regulated flow of helium gas.

Metal analysis. Metal analysis was carried out using inductively coupled plasma mass spectrometry (ICP–MS) as previously described[32,33].

Optical redox titration. Full spectrum UV–visible redox titrations were performed to determine the midpoint potentials (E_m°) of the redox-active cytochromes in the DDM-solubilized ACIII–cyt aa_3 supercomplex[34,35]. The purified supercomplex was suspended in 4 ml of 50 mM potassium phosphate buffer pH 7.0 to a concentration of 3 μM with 25 μM each of the following redox mediators: benzyl viologen ($E_{m,7} = -350$ mV), anthraquinone-2-sulfonate ($E_{m,7} = -225$ mV), 2-hydroxy-1,4-naphthoquinone ($E_{m,7} = -220$ mV), 9,10-anthroquinone-2,6-disulfonate ($E_{m,7} = -185$ mV), duroquinone ($E_{m,7} = 5$ mV), *N*-ethylphenazonium ethosulfate ($E_{m,7} = 65$ mV), *N*-methylphenazonium methosulfate ($E_{m,7} = 85$ mV), diaminodurene ($E_{m,7} = 275$ mV), 2,6-dimethyl benzoquinone ($E_{m,7} = 180$ mV), 1,2-napthoquinone ($E_{m,7} = 143$ mV), 1,4-napthoquinone ($E_{m,7} = 36$ mV) and potassium ferricyanide ($E_{m,7} = 435$ mV)[36].Titrations were performed with an anaerobic stirred cuvette and the solution potential was adjusted by injecting aliquots of 10 mM sodium dithionite or potassium ferricyanide as reductant and oxidant, respectively. Spectra were taken at approximately 10–20-mV increments over the titration range indicated. Spectroscopic changes of the α-bands of the haems upon reduction or oxidation were monitored at the peak maxima to determine the midpoint potentials of each class of haem centre. The datasets were analysed using Origin (Origin Laboratory Corporation) to determine spectral components and fit titration curves using the Nernst equation[36].

Electron microscopy sample preparation. Holey carbon film-coated electron microscopy grids were nanofabricated with regular arrays of 500- to 800-nm holes[37] and coated with an additional layer of gold. Cryo-EM specimens were prepared with a FEI Vitrobot grid preparation robot at 4 °C and 100% humidity by applying 3 μl of sample (3 mg ml^{-1}) to glow-discharged grids, allowing the grids to equilibrate for 1 s, and blotting for 12 s before freezing in a liquid ethane:propane mixture (1:1 v/v)[38]. Grids were subsequently stored in liquid nitrogen before shipping to the New York Structural Biology Center for imaging with a FEI Titan Krios electron microscope equipped with a Gatan K2 Summit camera and automated with Leginon[39].

Electron microscopy data acquisition. Movies were acquired in electron counting mode with a pixel size of 1.1 Å, an exposure rate of 7.4 electrons per pixel per second, and a total exposure time of 10 s divided in 40 frames (418 movies) or 50 frames (1,599 movies). Frame alignment and exposure weighting were performed with Motioncor2[40]. After screening averages from the aligned movies, 475 movies were discarded because of excessive movement, low defocus, high defocus, or overfocus. Contrast transfer function parameters were estimated from the exposure-weighted averages of movie frames with CTFFIND4[41].

Image processing. Particle images (3,044) were manually selected and subjected to 2D classification with Relion 1.4[42]. The resulting 2D classes were used as templates for automatic selection of 899,405 particle images[43]. The number of particle images was reduced to 693,416 by further 2D classification. Subsequent image processing was carried out in cryoSPARC[44]. An initial map of ACIII–cyt aa_3 was obtained

by ab initio 3D classification, refined to 4.1 Å resolution, and used as a reference for the multi-refine procedure in cryoSPARC producing initial maps of the ACIII and the ACIII–cyt aa_3. Particle images (164,239) were used to refine the ACIII–cyt aa_3 map to 3.4 Å resolution, but this map showed the cyt aa_3 portion of the complex with lower density than the ACIII part. Maps with uniform density for ACIII–cyt aa_3 and ACIII, both at 3.6 Å resolution, were calculated from 81,530 and 51,547 particle images, respectively.

Model building. The 3.4 Å resolution density map was used for the de novo model building of ACIII. The density map was first segmented with UCSF Chimera[45] to facilitate the identification of subunits. The connectivity of each segmented map was further examined and the result was compared with topology predictions from topocons[46] and secondary structure prediction from Jpred[47] to validate the subunit assignment and identify the directionality of peptide chain. With this information, model building was carried out manually in Coot[48]. Individual chains were first traced in Cα baton mode. Readily interpretable features from the density map, including regions rich in bulky residues, triacylated cysteines, and axial ligands of haem *c*, were used to register the structure to the sequence. Stretches of ~20 amino acids were built progressively around these registration points and assembled as a single chain in Coot. All six subunits of ACIII were combined and refined with phenix.real_space_refine[49]. For cofactors, the starting models were taken from the CCP4 ligand library directly. Cofactors were docked to the density map with Coot and merged with the apo protein structure. The complete structure was then refined with phenix.real_space_refine with geometric constraints for the protein–cofactor coordination. The final model was further examined in Coot to remove amino acid side chains with ambiguous orientations and further validated with MolProbity[50] and EMringer[51]. All identified lipids with two acyl tails were modelled as phosphatidylethanolamine with palmitoyl tail. The conformation of phosphatidylethanolamine was refined with interactive molecular dynamics flexible fitting (iMDFF) in the presence of the protein structure using VMD[52]. Lipid tails were then truncated according to the density map.

The 3.6 Å resolution ACIII–cyt aa_3 density map was used for the model building of cyt aa_3. Part of the subunit III loop region was manually built in *Coot*. Homology models for individual subunits were generated with the RaptorX server[53] and docked into the density map with UCSF Chimera. The model for the ACIII–cyt aa_3 supercomplex was assembled by fitting the ACIII structure to the ACIII–cyt aa_3 map and placing the cyt aa_3 structure from *Rba. sphaeroides* (PDB 1M56) into the map based on the position of cyt aa_3 subunit III.

Bioinformatic analysis. Homologous protein sequences were retrieved using the NCBI blastp server[54]. The blastp results were analysed in python 2.7 with pandas and biopython modules. Sequence hits were filtered on the basis of coverage and sequence identity. Representative sequences were selected on the basis of sequence identity to maintain the variations in sequence and aligned using the Clustal Omega server[55]. Figures for sequence alignment were prepared using the ESPript 3.0 server[56].

Simulation system preparation. The initial ACIII structure for the MD simulation was obtained from the refined structure determined by cryo-EM. Eleven 1-palmitoyl-2-oleoyl-*sn*-glycero-3-phosphoethanolamine (POPE) lipids resolved by cryo-EM were added to the ACIII system, which was subsequently embedded in a POPE membrane bilayer, solvated with the TIP3P water model[57], and ionized with 150 mM NaCl.

ReMDFF simulation. Resolution-exchange molecular dynamics flexible fitting (ReMDFF)[58] was used for structure refinement, with the CHARMM36m force field for proteins[59] and the CHARMM36 force field for lipids[60]. Force-field parameters for haems and iron–sulfur clusters came from previous studies[61–63]. The fitting was performed in vacuum in the presence of a grid potential derived from the experimental density map (coupling factor 0.3). Secondary structure restraints, *cis*-peptide bond restraints, and chirality restraints were applied to the protein. Haems and iron–sulfur clusters were harmonically restrained ($k = 50$ kcal mol^{-1} Å^{-2}). A Langevin thermostat[64] was used for maintaining the average temperature at 80 K. The MD integration time step was 1 fs. A cut-off radius for nonbonded interactions was set to 10 Å with a switching function taking effect at 9 Å. A total of six replicas were used together with six grid potentials of decreasing resolution. Each was first energy-minimized for 2,000 steps and then equilibrated for 1 ps. Finally, 2,000 replica exchanges were attempted with 1 ps between attempts.

Molecular dynamics simulation. The ACIII systems were simulated with *NAMD* 2.12 using the same force-field parameters as in ReMDFF. The system was energy-minimized for 3,000 steps using the conjugated gradient algorithm[65] with linear searching[66], and equilibrated for 0.5 ns to relax lipid tail group atoms while keeping the lipid phosphorus atoms and protein (including haems and iron–sulfur clusters) heavy atoms harmonically restrained ($k = 1$ kcal mol^{-1} Å^{-2}). This procedure was followed by a 10-ns simulation to allow lipids to relax around the proteins while keeping the protein backbone and heavy atoms from iron–sulfur clusters and haems harmonically restrained ($k = 1$ kcal mol^{-1} Å^{-2}). Restraints were gradually released over the next 5 ns and the simulation continued without any biasing potential for a total of 250 ns. The angles in the iron–sulfur clusters were harmonically restrained to their initial values ($k = 300$ kcal mol^{-1} deg^{-1}) throughout the simulation.

Reporting summary. Further information on experimental design is available in the Nature Research Reporting Summary linked to this paper.

Data availability. All relevant data are included in the manuscript or Supplementary Information and/or are available from the corresponding authors upon reasonable request. Three cryo-EM maps mentioned in this work have been deposited in the Electron Microscopy Data Bank (EMDB) under accession codes EMD-7286 (combined), EMD-7447 (ACIII–cyt aa_3), EMD-7448 (ACIII). The coordinates of the atomic model of the alternative complex III built from EMD-7286 have been deposited in the Protein Data Bank (PDB) under accession code 6BTM.

25. McBride, M. J. & Baker, S. A. Development of techniques to genetically manipulate members of the genera *Cytophaga, Flavobacterium, Flexibacter*, and *Sporocytophaga*. *Appl. Environ. Microbiol.* **62**, 3017–3022 (1996).
26. Bell, A. J., Frankel, L. K. & Bricker, T. M. High yield non-detergent isolation of photosystem I-light-harvesting chlorophyll II membranes from spinach thylakoids: implications for the organization of the PS I antennae in higher plants. *J. Biol. Chem.* **290**, 18429–18437 (2015).
27. Berry, E. A. & Trumpower, B. L. Simultaneous determination of hemes *a*, *b*, and *c* from pyridine hemochrome spectra. *Anal. Biochem.* **161**, 1–15 (1987).
28. Thomas, P. E., Ryan, D. & Levin, W. An improved staining procedure for the detection of the peroxidase activity of cytochrome P-450 on sodium dodecyl sulfate polyacrylamide gels. *Anal. Biochem.* **75**, 168–176 (1976).
29. Minghetti, K. C. et al. Modified, large-scale purification of the cytochrome *o* complex (*bo*-type oxidase) of *Escherichia coli* yields a two heme/one copper terminal oxidase with high specific activity. *Biochemistry* **31**, 6917–6924 (1992).
30. Gao, X., Xin, Y. & Blankenship, R. E. Enzymatic activity of the alternative complex III as a menaquinol:auracyanin oxidoreductase in the electron transfer chain of *Chloroflexus aurantiacus*. *FEBS Lett.* **583**, 3275–3279 (2009).
31. Ragan, C. I., Wilson, M. T., Darley-Usmar, V. M. & Lowe, P. N. *Mitochondria: A Practical Approach* (IRL Press, Oxford, 1987).
32. Carrell, C. J. et al. Generation of novel copper sites by mutation of the axial ligand of amicyanin. Atomic resolution structures and spectroscopic properties. *Biochemistry* **46**, 1900–1912 (2007).
33. Ouyang, H. et al. Functional importance of a pair of conserved glutamic acid residues and of Ca^{2+} binding in the cbb_3-type oxygen reductases from *Rhodobacter sphaeroides* and *Vibrio cholerae*. *Biochemistry* **51**, 7290–7296 (2012).
34. Bowyer, J. R., Tierney, G. V. & Crofts, A. R. Cytochrome c_2 – reaction centre coupling in chromatophores of *Rhodopseudomonas sphaeroides* and *Rhodopseudomonas capsulata*. *FEBS Lett.* **101**, 207–212 (1979).
35. Dutton, P. L. Redox potentiometry: determination of midpoint potentials of oxidation-reduction components of biological electron-transfer systems. *Methods Enzymol.* **54**, 411–435 (1978).
36. Fultz, M. & Durs, R. Mediator compounds for the electrochemical study of biological redox systems: a compilation. *Anal. Chim. Acta* **140**, 1–18 (1982).
37. Marr, C. R., Benlekbir, S. & Rubinstein, J. L. Fabrication of carbon films with ~500 nm holes for cryo-EM with a direct detector device. *J. Struct. Biol.* **185**, 42–47 (2014).
38. Tivol, W. F., Briegel, A. & Jensen, G. J. An improved cryogen for plunge freezing. *Microsc. Microanal.* **14**, 375–379 (2008).
39. Suloway, C. et al. Automated molecular microscopy: the new Leginon system. *J. Struct. Biol.* **151**, 41–60 (2005).
40. Zheng, S. Q. et al. MotionCor2: anisotropic correction of beam-induced motion for improved cryo-electron microscopy. *Nat. Methods* **14**, 331–332 (2017).
41. Rohou, A. & Grigorieff, N. CTFFIND4: Fast and accurate defocus estimation from electron micrographs. *J. Struct. Biol.* **192**, 216–221 (2015).
42. Scheres, S. H. W. A Bayesian view on cryo-EM structure determination. *J. Mol. Biol.* **415**, 406–418 (2012).
43. Scheres, S. H. W. Semi-automated selection of cryo-EM particles in RELION-1.3. *J. Struct. Biol.* **189**, 114–122 (2015).
44. Punjani, A., Rubinstein, J. L., Fleet, D. J. & Brubaker, M. A. cryoSPARC: algorithms for rapid unsupervised cryo-EM structure determination. *Nat. Methods* **14**, 290–296 (2017).
45. Pettersen, E. F. et al. UCSF Chimera—a visualization system for exploratory research and analysis. *J. Comput. Chem.* **25**, 1605–1612 (2004).
46. Tsirigos, K. D., Peters, C., Shu, N., Käll, L. & Elofsson, A. The TOPCONS web server for consensus prediction of membrane protein topology and signal peptides. *Nucleic Acids Res.* **43**, W401–W407 (2015).
47. Drozdetskiy, A., Cole, C., Procter, J. & Barton, G. J. JPred4: a protein secondary structure prediction server. *Nucleic Acids Res.* **43**, W389–W394 (2015).
48. Emsley, P., Lohkamp, B., Scott, W. G. & Cowtan, K. Features and development of *Coot*. *Acta Crystallogr. D* **66**, 486–501 (2010).
49. Adams, P. D. et al. PHENIX: a comprehensive Python-based system for macromolecular structure solution. *Acta Crystallogr. D* **66**, 213–221 (2010).
50. Chen, V. B. et al. MolProbity: all-atom structure validation for macromolecular crystallography. *Acta Crystallogr. D* **66**, 12–21 (2010).
51. Barad, B. A. et al. EMRinger: side chain-directed model and map validation for 3D cryo-electron microscopy. *Nat. Methods* **12**, 943–946 (2015).

52. Humphrey, W., Dalke, A. & Schulten, K. VMD: visual molecular dynamics. *J. Mol. Graph.* **14**, 33–38 (1996).
53. Källberg, M. et al. Template-based protein structure modeling using the RaptorX web server. *Nat. Protoc.* **7**, 1511–1522 (2012).
54. Madden, T. L., Tatusov, R. L. & Zhang, J. Applications of network BLAST server. *Methods Enzymol.* **266**, 131–141 (1996).
55. Sievers, F. et al. Fast, scalable generation of high-quality protein multiple sequence alignments using Clustal Omega. *Mol. Syst. Biol.* **7**, 539 (2011).
56. Robert, X. & Gouet, P. Deciphering key features in protein structures with the new ENDscript server. *Nucleic Acids Res.* **42**, W320–W324 (2014).
57. Jorgensen, W. L., Chandrasekhar, J., Madura, J. D., Impey, R. W. & Klein, M. L. Comparison of simple potential functions for simulating liquid water. *J. Chem. Phys.* **79**, 926–935 (1983).
58. Singharoy, A. et al. Molecular dynamics-based refinement and validation for sub-5 Å cryo-electron microscopy maps. *eLife* **5**, 61–67 (2016).
59. Huang, J. et al. CHARMM36m: an improved force field for folded and intrinsically disordered proteins. *Nat. Methods* **14**, 71–73 (2017).
60. Best, R. B. et al. Optimization of the additive CHARMM all-atom protein force field targeting improved sampling of the backbone φ, ψ and side-chain $\chi(1)$ and $\chi(2)$ dihedral angles. *J. Chem. Theory Comput.* **8**, 3257–3273 (2012).
61. Autenrieth, F., Tajkhorshid, E., Baudry, J. & Luthey-Schulten, Z. Classical force field parameters for the heme prosthetic group of cytochrome c. *J. Comput. Chem.* **25**, 1613–1622 (2004).
62. Autenrieth, F., Tajkhorshid, E., Klaus Schulten, A. & Luthey-Schulten, Z. Role of water in transient cytochrome c_2 docking. *J. Phys. Chem. B* **108**, 20376–20387 (2004).
63. Carvalho, A. T. P. & Swart, M. Electronic structure investigation and parametrization of biologically relevant iron–sulfur clusters. *J. Chem. Inf. Model.* **54**, 613–620 (2014). erratum 55, 1508–1508 (2015).
64. Allen, M. P. & Tildesley, D. J. *Computer Simulation of Liquids* (Oxford Univ. Press, New York, 1987).
65. Fletcher, R. & Reeves, C. M. Function minimization by conjugate gradients. *Comput. J.* **7**, 149–154 (1964).
66. Sun, W. & Yuan, Y.-X. *Optimization Theory and Methods: Nonlinear Programming* (Springer, New York, 2006).

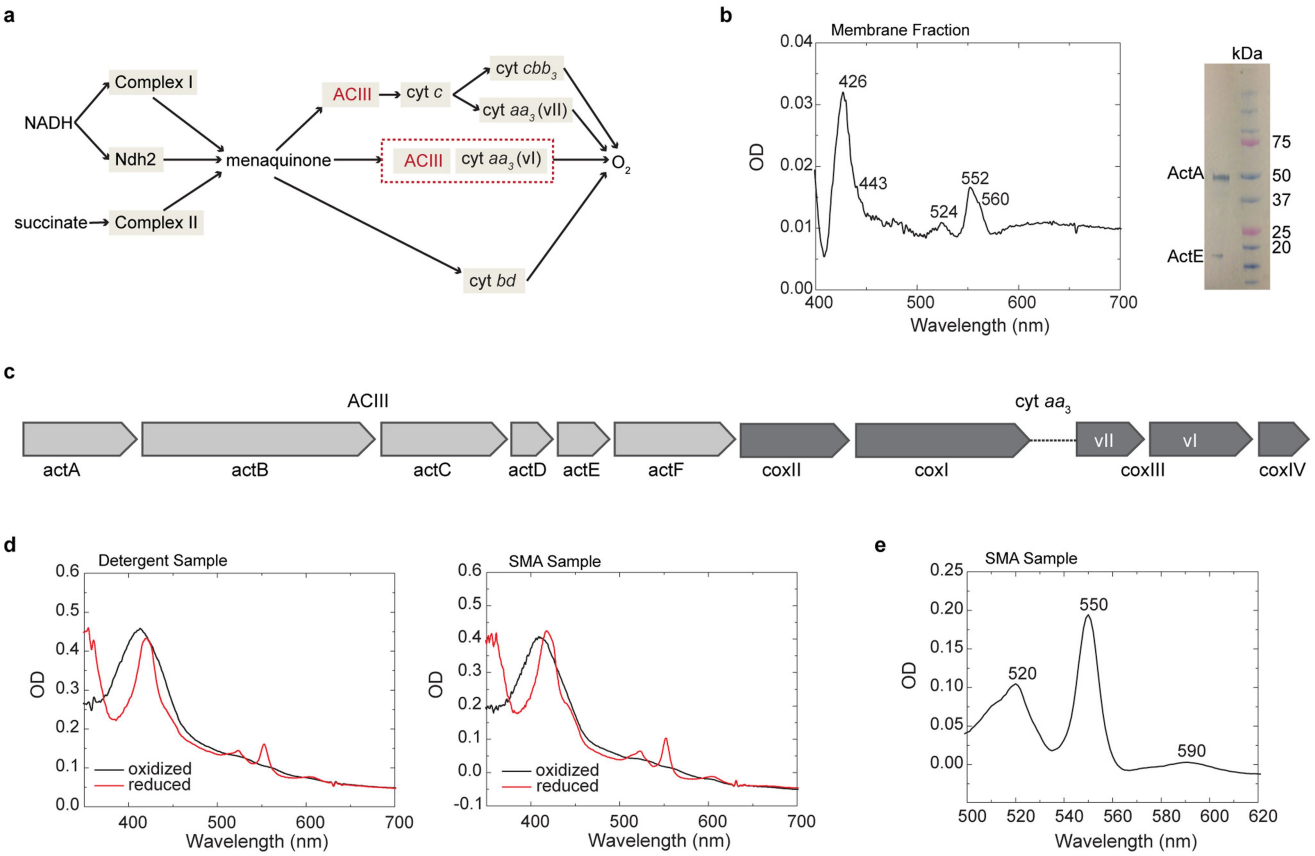

Extended Data Fig. 1 | Expression and spectroscopic characterization of the ACIII-cyt aa_3 supercomplex. a, A schematic of the respiratory chain of *F. johnsoniae*. **b**, UV–visible spectrum and SDS–PAGE of the membranes from *F. johnsoniae*. Left, the difference spectrum of the membranes of *F. johnsoniae*, obtained from the spectrum of the air-oxidized membranes and the spectrum after reduction with dithionite. The wavelengths associated with the haem peaks are 605 nm, 560 nm, 552 nm and a broad peak at 630 nm for haems *a, b, c* and *d*, respectively. Right, the SDS–PAGE with the membranes followed by staining the gel for haems shows bands corresponding to the cytochrome subunits ActA (48 kDa) and ActE (20 kDa) of ACIII but no bands corresponding to the cytochrome subunit (around 35 kDa) from the cbb_3 oxidase. **c**, The gene arrangement for the ACIII and the cytochrome oxidase aa_3 genes in the *F. johnsoniae* genome. The genes for the subunits I and II from cyt aa_3 oxidase are found immediately downstream of those for the *act* genes of the ACIII. Two different versions of subunit III are denoted as vI and vII. **d**, UV–visible spectra of the reduced and oxidized forms of the supercomplex in detergent and SMA nanodiscs. The dithionite reduced form of the samples is represented in red and shows the peaks for haem *c* at 524 nm and 552 nm and those for haem *a* at 443 nm and 605 nm. **e**, Pyridine haemochrome assay of the ACIII–cyt aa_3 supercomplex in SMA nanodiscs. Plotted is the reduced-minus-oxidized difference spectrum of the pyridine haemochromes of the sample. Peaks at 520 nm and 550 nm are associated with haem *c* and the peak at 590 nm is associated with haem *a*. Quantification from the spectrum shows a ratio of 10.6:1 between haem *c* and haem *a*, which translates into a 3:2 ratio between ACIII and cyt aa_3 assuming 7 haem *c* per ACIII and 2 haem *a* per cyt aa_3. Data in **b** are representative of two independent experiments with similar results, and data in **d** and **e** are representative of six independent experiments with similar results.

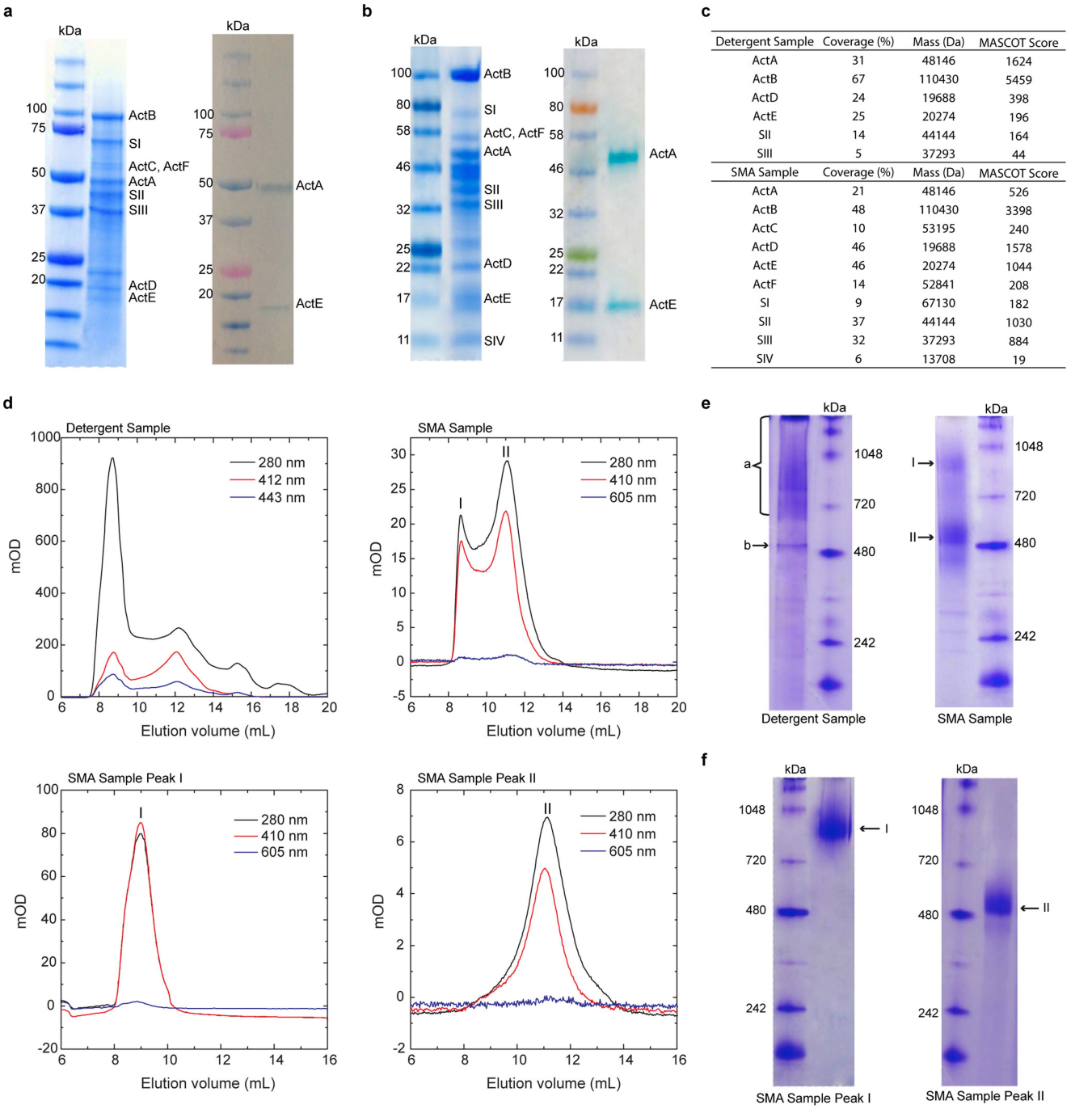

Detergent Sample	Coverage (%)	Mass (Da)	MASCOT Score
ActA	31	48146	1624
ActB	67	110430	5459
ActD	24	19688	398
ActE	25	20274	196
SII	14	44144	164
SIII	5	37293	44
SMA Sample	**Coverage (%)**	**Mass (Da)**	**MASCOT Score**
ActA	21	48146	526
ActB	48	110430	3398
ActC	10	53195	240
ActD	46	19688	1578
ActE	46	20274	1044
ActF	14	52841	208
SI	9	67130	182
SII	37	44144	1030
SIII	32	37293	884
SIV	6	13708	19

Extended Data Fig. 2 | Component and size analysis of ACIII–cyt aa_3 supercomplex. a, SDS–PAGE of the detergent-solubilized preparation followed by Coomassie staining (left) and haem staining (right). **b**, SDS–PAGE of the SMA nanodiscs preparation followed by Coomassie staining (left) and haem staining (right). **c**, Mass spectrometry results for the ACIII–cyt aa_3 supercomplex preparations. **d**, Size-exclusion chromatography with the ACIII–cyt aa_3 supercomplex from *F. johnsoniae*. Top left, the chromatogram of the detergent-solubilized sample, showing traces for protein at 280 nm, haem *c* at 412 nm and haem *a* at 443 nm respectively. Top right, the chromatogram of the sample isolated using the SMA copolymer, showing traces for protein at 280 nm, haem *c* at 410 nm and haem *a* at 605 nm. I and II are the two peaks corresponding to two populations of the supercomplex. Bottom left, chromatogram of the fraction containing peak I. Bottom right, chromatogram of the fraction containing peak II. **e**, BN–PAGE of the ACIII–cyt aa_3 supercomplex. Left, the detergent-solubilized ACIII–cyt aa_3 supercomplex, showing a band at around 500 kDa, a smear of possible aggregates and possibly ACIII by itself. Right, the supercomplex in SMA nanodiscs, showing two different populations. **f**, BN–PAGE with the two different populations of ACIII–cyt aa_3 supercomplex in SMA nanodiscs purified from size-exclusion chromatography. The two chromatographic peaks correspond to the two bands observed in the BN–PAGE. Data in **a**, **b** are representative of six independent experiments and those in **d**–**f** are representative of three independent experiments with similar results.

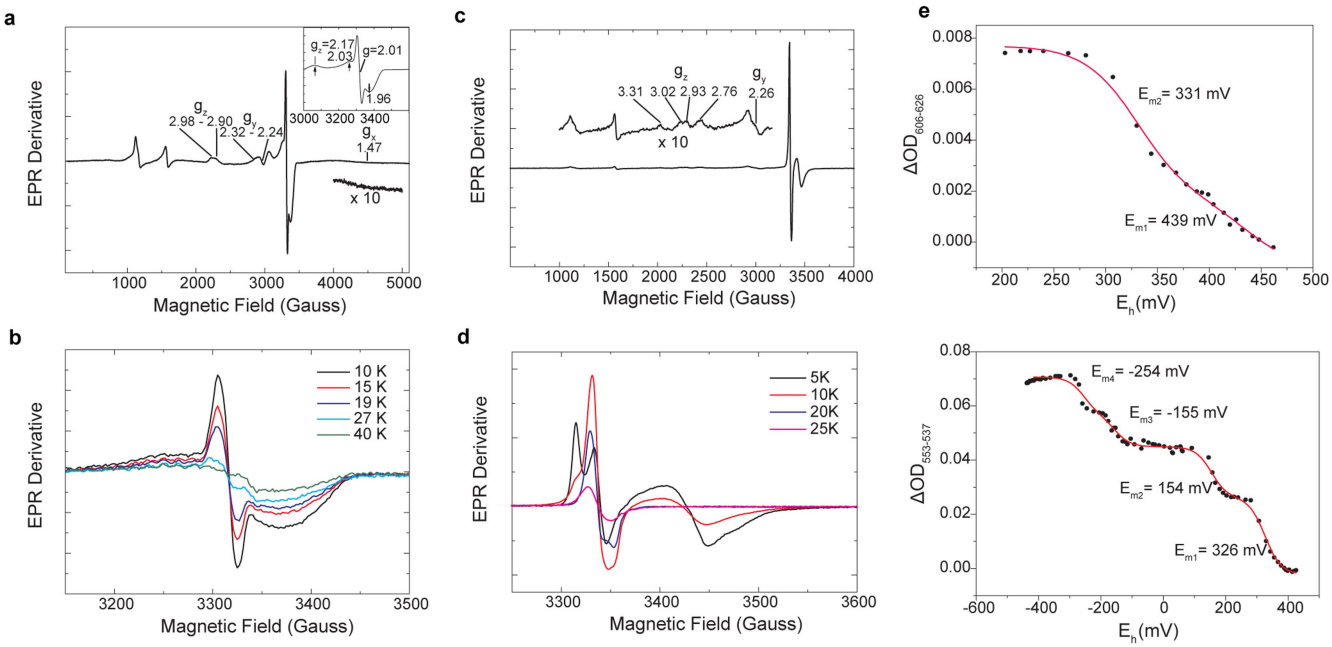

f

	k_{cat} ($Q_1H_2 \rightarrow O_2$) (electrons s^{-1})	k_{cat} ($Q_1H_2 \rightarrow$cyt *c*) (electrons s^{-1})	k_{cat} ($MK_4H_2 \rightarrow$cyt *c*) (electrons s^{-1})
ACIII in DDM	15 ± 0.5	1.6 ± 0.1	20 ± 0.6
ACIII in SMA nanodisc	22 ± 1	N.D.	5 ± 1
ACIII in SMA nanodisc Peak I after SEC	21 ± 0.3	-	-
ACIII in SMA nanodisc Peak II after SEC	22 ± 0.5	-	-

Extended Data Fig. 3 | Functional assays of the ACIII–cyt aa_3 supercomplex. a, The EPR spectrum of the air-oxidized sample showing peaks of the $[3Fe–4S]^+$ cluster from ACIII, the Cu_A from the cyt aa_3 oxidase and low-spin haems with overlapping *g* values. Insert is a zoomed view from 3,000 G to 3,500 G to better visualize the peaks from Cu_A (black arrows) and the $[3Fe–4S]^+$ cluster. The region between 4,000 G and 5,000 G is magnified ten times to show the broad g_x trough of low-spin haems. The measurement condition is 10 K, 9.267 GHz, 2 mW microwave power and 20 Gauss modulation. **b**, The EPR spectra of the ferricyanide-oxidized sample at various temperatures. The measurement condition is 9.257 GHz, 2 mW microwave power and 5 Gauss modulation. **c**, The EPR spectrum of the air-oxidized sample showing peaks of iron–sulfur clusters from ACIII and low-spin haems. The measurement condition is 10 K, 9.427 GHz, 2 mW microwave power, 10 Gauss modulation. **d**, The EPR spectra of the air-oxidized sample at various temperatures. The measurement condition is 9.427 GHz, 2 mW microwave power, 5 Gauss modulation. **e**, Redox titration of the haems in the ACIII and the cyt aa_3 oxidase in supercomplex in DDM. The potentiometric titration of the *c* haems from the ACIII (top) and the *a* haems from the cyt aa_3 oxidase (bottom). The E_m values are indicated and the solid red line represents the Nernst fitting. **f**, Steady-state activity of the ACIII–cyt aa_3 preparations. The number of independent experiments is six for ACIII in DDM and SMA nanodiscs, and three for peak I and peak II. Data are means ± s.d. Data in **a**–**e** are representative of three independent experiments with similar results.

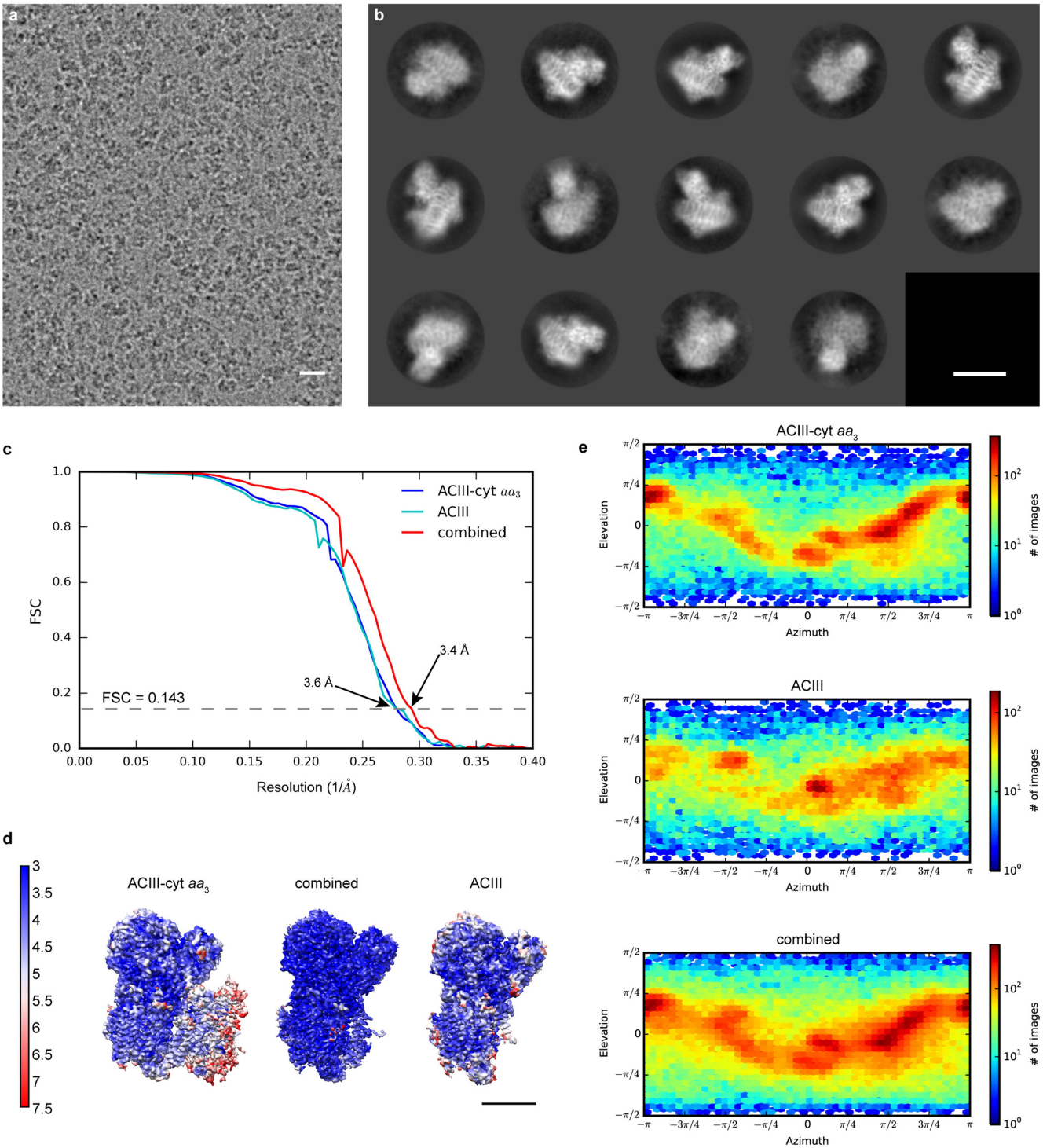

Extended Data Fig. 4 | Single-particle cryo-EM of the ACIII–cyt aa_3 supercomplex in SMA nanodiscs. a, Sum of an aligned movie of the ACIII–cyt aa_3 supercomplex in an SMA nanodisc. Scale bar, 20 nm. **b**, Two-dimensional class averages. Scale bar, 10 nm. **c**, Fourier shell coefficient curves between two independently refined half-maps for the ACIII–cyt aa_3 map, ACIII map and combined map. **d**, Surface rendering maps coloured according to local resolution. Scale bar, 5 nm. **e**, Euler angle distributions of particles included in the calculation of the three final maps. Data collection and structure calculation were not repeated.

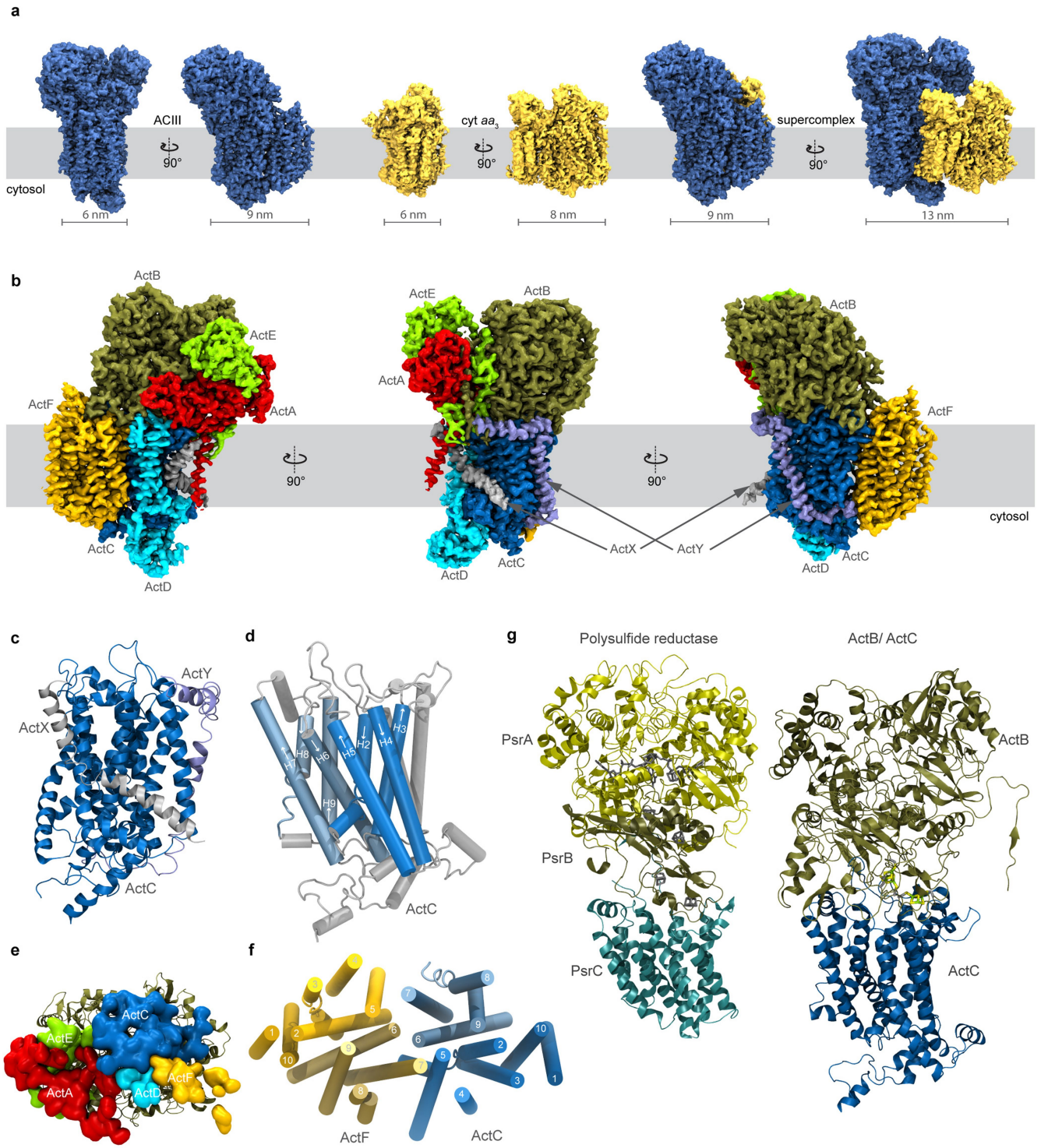

Extended Data Fig. 5 | Features observed in the cryo-EM density and the de novo structure of ACIII. a, Surface representations of ACIII, cyt aa_3 and the ACIII–cyt aa_3 supercomplex. The density threshold is the same for ACIII and cyt aa_3. **b**, Different views of the ACIII density, coloured by subunit. **c**, Two single-span transmembrane peptides of unknown origin and sequence, denoted ActX and ActY, are present in the structure in the vicinity of ActC. These have each been modelled as a polyalanine peptide. **d**, α-helices 2–10 of ActC form two four-helical up-and-down bundles, coloured in two different shades of blue. α-helices 1 and 10 are coloured grey and unlabelled. **e**, ActB, shown in cartoon form, has contact with ActA, ActC, ActD, ActE and ActF. Surfaces are drawn from residues that are within 4 Å of ActB and coloured according to their chain. **f**, The transmembrane α-helices of ActC and ActF are arranged in a pseudo two-fold rotation symmetry. **g**, Side-by-side comparison of the polysulfide reductase (PDB 2VPZ) and the assembly of ActB and ActC. These two structures are aligned based on PsrB, the domain containing four iron–sulfur clusters.

Extended Data Fig. 6 | The proposed quinone pocket in ActC. **a**, Sequence alignment of the ActC from *F. johnsoniae*, *R. marinus*, and *Chloroflexus aurantiacus*. The transmembrane α-helices are labelled based on the structure of ACIII from *F. johnsoniae*. The black arrows point to conserved polar residues that are within 15 Å of the [3Fe–4S] cluster in ActB. **b**, Proposed quinone pocket based on the arrangement of conserved polar residues. **c**, Different views of the proposed quinone pocket with a docked menaquinone-1 molecule. Hydrophobic residues near the menaquinone-1 (MK1) head group are also shown. The crevice between α-helix 3 and α-helix 4 is a putative quinone entry pathway.

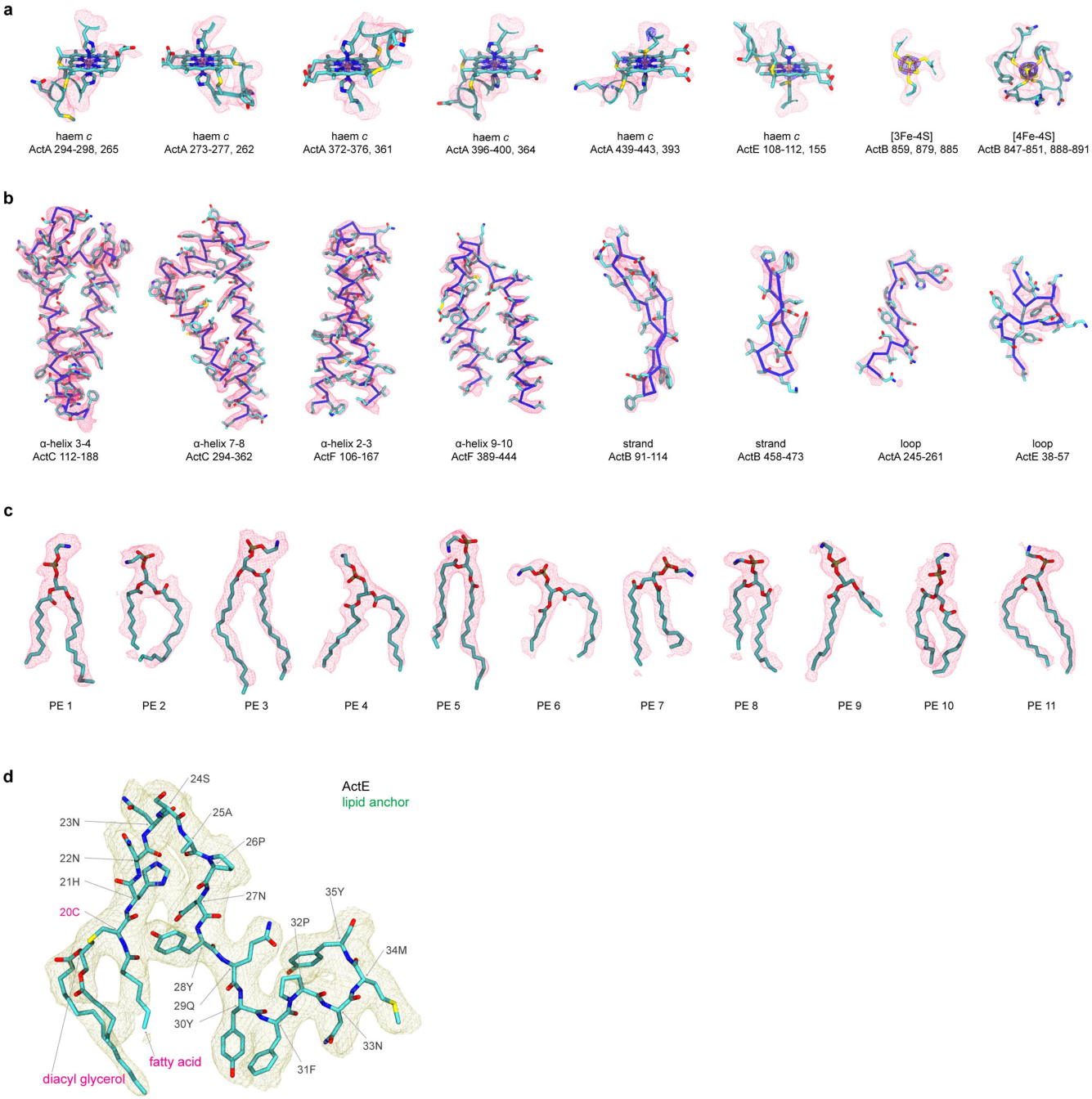

Extended Data Fig. 7 | Fitting of the ACIII structure to cryo-EM density. **a**, Fitting of cofactors into the cryo-EM density. The blue mesh is drawn with a higher density threshold to reveal metal centres. The numberings of nearby amino acid residues, which are shown along with these cofactors, are listed below each cofactor. **b**, Fitting of different secondary structure elements to cryo-EM density. **c**, Eleven identified lipids are modelled as phosphatidylethanolamine molecules. **d**, The triacylated cysteine at the N terminus of ActE shown along with 15 downstream amino acids. Notably, residue Tyr28 is in contact with the covalent lipid of ActE. Attachment of ActE to the membrane may also be assisted by aromatic residues Tyr30 and Phe31, which appear to be inserted into the lipid bilayer. Throughout the molecular dynamics simulation trajectory, these residues remain buried in the lipid bilayer.

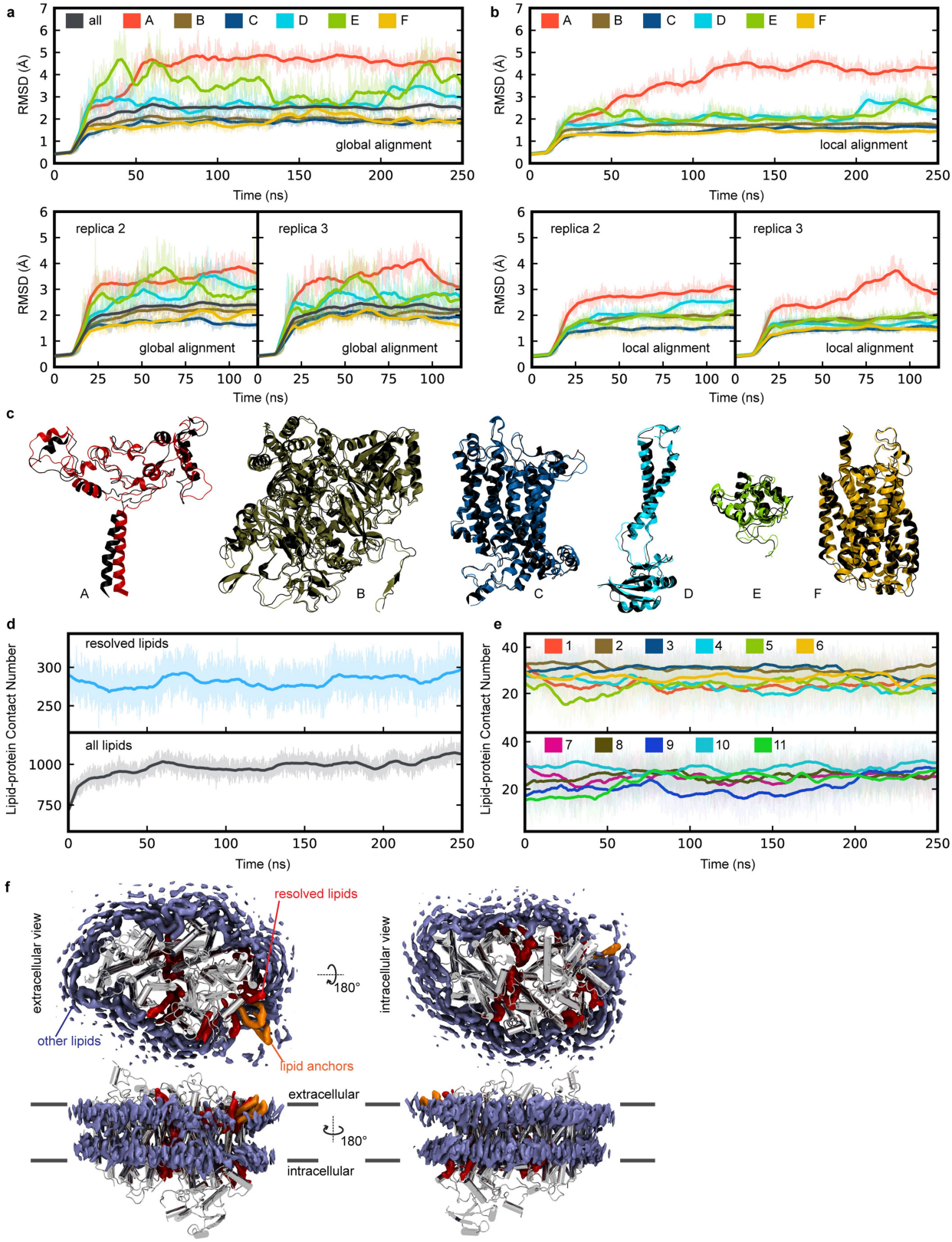

Extended Data Fig. 8 | Protein stability and lipid–protein interaction analysis based on molecular dynamics simulations. **a**, Root-mean-square deviation (r.m.s.d.) of the protein backbone heavy atoms for the entire ACIII complex and each subunit, aligned based on ACIII backbone heavy atoms from three independent molecular dynamics simulations. **b**, Same as **a**, but aligned using the backbone heavy atoms of each subunit. **c**, Superposition of the initial (black) and final (coloured) conformations of each subunit after 250 ns of simulation (aligned using backbone heavy atoms). **d**, The lipid–protein contact number defined by the number of lipid atoms within 4 Å of the protein atoms calculated over the time course of the simulation. This contact number is either calculated for the eleven lipids resolved by cryo-EM (top) or all membrane lipids (bottom). **e**, The lipid–protein contact number for each of the eleven cryo-EM resolved lipids. **f**, Isosurfaces (50%) of the atom-occupancy map for the lipid anchors (orange), cryo-EM resolved lipids (red) and other membrane lipids (purple), calculated using the last 230 ns of the simulation trajectory. The stronger the lipid–protein interactions, the longer the local residence time, which leads to higher atom-occupancy values. ACIII subunits C, D, and F are shown in silver. For all plots, the raw data are shown as translucent thin lines and the block-averages are shown as dark lines.

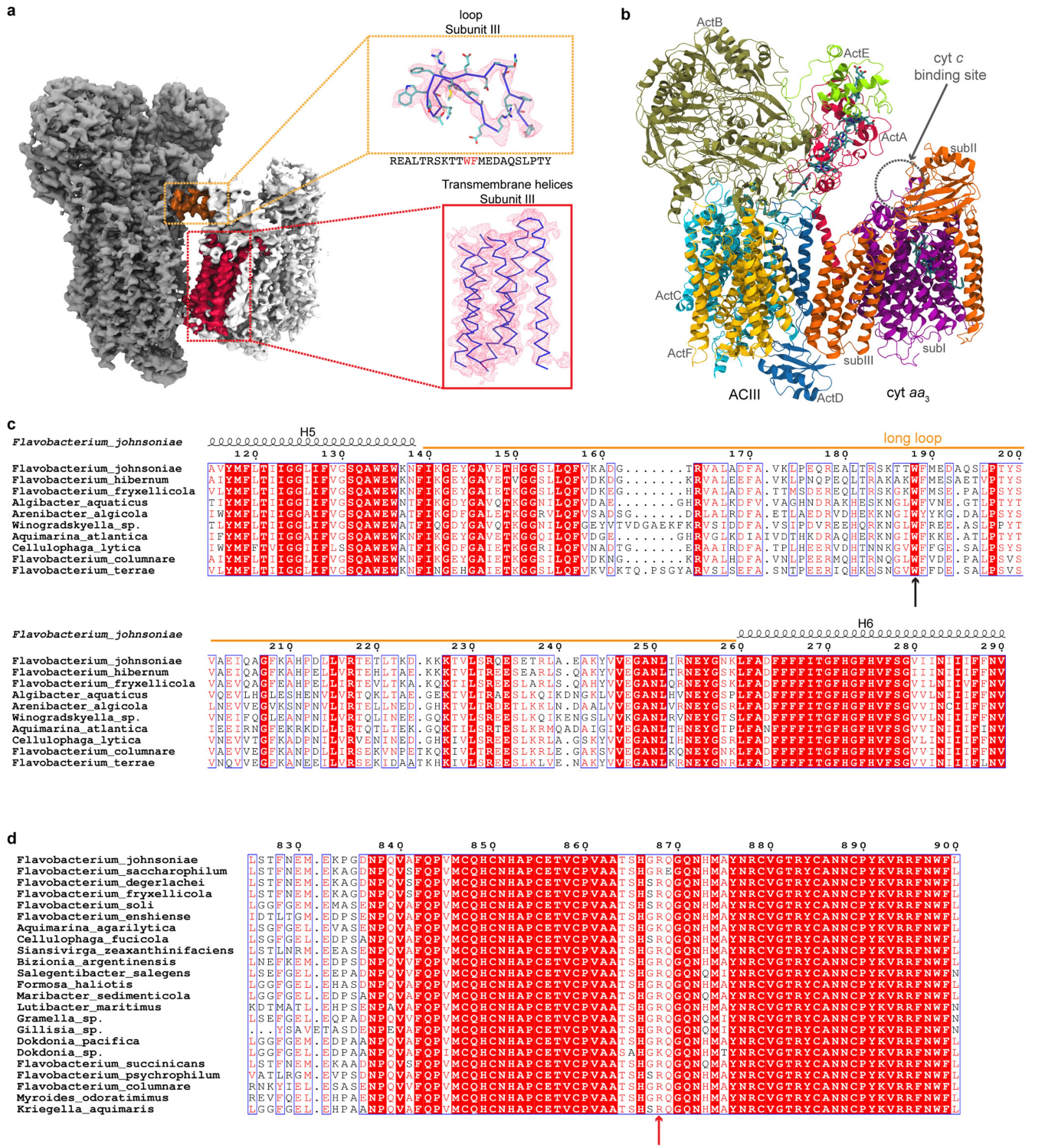

Extended Data Fig. 9 | Structural basis for supercomplex formation between the ACIII and the cyt aa_3. **a**, Two contact areas between the ACIII and the cyt aa_3: the transmembrane portion of subunit III (red) and the loop from subunit III (orange). A homology model of subunit III fits the transmembrane density. The loop is modelled to the cryo-EM density. The sequence of the peptide is also shown. Trp188 and Phe189 are used to register the density to the sequence. **b**, Model of the ACIII–cyt aa_3 supercomplex. The cyt aa_3 structure from *Rba. sphaeroides* was positioned based on the transmembrane portion of subunit III. α-helices 1 and 2 of subunit III are omitted to avoid steric clashes with the ACIII structure. **c**, Sequence alignment of subunit III with a long loop (highlighted with the orange bar) between α-helix 5 and α-helix 6 (numbered according to subunit III from *Rba. sphaeroides*). Trp188 (black arrow) is conserved. **d**, Sequence alignment of ActB from organisms with a long loop in subunit III of their cyt aa_3 oxidase. Arg868 (red arrow) is largely conserved with occasional substitution to lysine.

Extended Data Table 1 | Cryo-EM data collection, refinement and validation statistics

	Combined (EMDB-7286) (PDB 6BTM)	ACIII-cyt aa_3 (EMDB-7447)	ACIII (EMDB-7448)
Data collection and processing			
Magnification	75,000×	75,000×	75,000×
Voltage (kV)	300	300	300
Electron exposure (e^{-}/Å^2)	61	61	61
Defocus range (μm)	0.8-5.0	0.8-5.0	0.8-5.0
Pixel size (Å)	1.1	1.1	1.1
Symmetry imposed	C1	C1	C1
Initial particle images (no.)	899,405	899,405	899,405
Final particle images (no.)	164,239	81,530	51,547
Map resolution (Å)	3.4*	3.6*	3.6*
FSC threshold	0.143	0.143	0.143
Map resolution range (Å)	3.0-4.5	3.0-6.0	3.0-5.0
Refinement			
Initial model used (PDB code)	N/A	N/A	N/A
Model resolution (Å)	3.7†	N/A	N/A
FSC threshold	0.5		
Model resolution range (Å)	3.7	N/A	N/A
Map sharpening *B* factor (Å^2)	-150.1	-132.4	-129.1
Model composition			
Non-hydrogen atoms	18,935		
Protein residues	2,361		
Ligands	10		
B factors (Å^2)			
Protein	126.4‡		
Ligand	119.7‡		
R.M.S. deviations			
Bond lengths (Å)	0.009		
Bond angles (°)	1.26		
Validation			
MolProbity score	1.36		
Clashscore	1.58		
Poor rotamers (%)	0.15		
Ramachandran plot			
Favored (%)	92.7		
Allowed (%)	7.3		
Disallowed (%)	0.0		

*Determined with cryoSPARC
†Determined with Phenix.mtriage
‡Mean value of the B factors determined with Phenix.real_space_refine

nature research

Corresponding author(s): Robert B Gennis

☐ Initial submission ☐ Revised version ☒ Final submission

Life Sciences Reporting Summary

Nature Research wishes to improve the reproducibility of the work that we publish. This form is intended for publication with all accepted life science papers and provides structure for consistency and transparency in reporting. Every life science submission will use this form; some list items might not apply to an individual manuscript, but all fields must be completed for clarity.

For further information on the points included in this form, see Reporting Life Sciences Research. For further information on Nature Research policies, including our data availability policy, see Authors & Referees and the Editorial Policy Checklist.

Experimental design

1. Sample size

Describe how sample size was determined.

No statistical methods were used to predetermine sample size. The sample size was chosen following the guidelines from the instrument manufacturer.

2. Data exclusions

Describe any data exclusions.

A fraction of the acquired cryo-EM movies were discarded because of excessive movement, low defocus, high defocus, or over-focus.

3. Replication

Describe whether the experimental findings were reliably reproduced.

cyro-EM Data collection and structure calculation were not repeated.

4. Randomization

Describe how samples/organisms/participants were allocated into experimental groups.

Samples were not allocated into experimental groups because the goal of this study was not to evaluate the impact of a particular factor, but to simply determine the structure of a protein.

5. Blinding

Describe whether the investigators were blinded to group allocation during data collection and/or analysis.

Not applicable. There was no existing protein structure to refer to and the data analysis was ab initio.

Note: all studies involving animals and/or human research participants must disclose whether blinding and randomization were used.

6. Statistical parameters

For all figures and tables that use statistical methods, confirm that the following items are present in relevant figure legends (or in the Methods section if additional space is needed).

n/a	Confirmed	
☒	☐	The exact sample size (*n*) for each experimental group/condition, given as a discrete number and unit of measurement (animals, litters, cultures, etc.)
☒	☐	A description of how samples were collected, noting whether measurements were taken from distinct samples or whether the same sample was measured repeatedly
☒	☐	A statement indicating how many times each experiment was replicated
☒	☐	The statistical test(s) used and whether they are one- or two-sided (note: only common tests should be described solely by name; more complex techniques should be described in the Methods section)
☒	☐	A description of any assumptions or corrections, such as an adjustment for multiple comparisons
☒	☐	The test results (e.g. *P* values) given as exact values whenever possible and with confidence intervals noted
☒	☐	A clear description of statistics including central tendency (e.g. median, mean) and variation (e.g. standard deviation, interquartile range)
☒	☐	Clearly defined error bars

See the web collection on statistics for biologists for further resources and guidance.

Software

Policy information about availability of computer code

7. Software

Describe the software used to analyze the data in this study.	Leginon as of February 2017 used in Simons Electron Microscopy Center at New York to collect cryo-EM movies; Motioncor2 to align frames and weigh exposure; CTFFIND4 to estimate CTF parameters; Relion 1.4, cryoSPARC 0.3.2 to process images and reconstruct cryo-EM density maps; Jpred 4 server to predict protein secondary structures; Topocons server to predict membrane protein topology; RaptorX server to build homology-based protein structures; NCBI blastp server to retrieve homologous protein sequences; python 2.7.13, pandas 0.20.1, biopython 1.68 to analyze/filter protein sequences Clustal Omega server to align protein sequences; ESPript 3.0 server to represent protein sequence alignments; UCSF Chimera 1.12, Coot 0.8.8 EL (ccp4) to examine density map and build atomic structures; MDFF, Phenix.real_space_refine (Phenix ver-2722), modelmaker (beta version) to refine atomic structures; EMringer, MolProbity and Phenix.mtriage (Phenix ver-2998) to validate atomic structures; namd 2.13 to run molecular dynamics simulations; VMD 1.9.4, Origin 9.1, matplotlib 1.5.1, Adobe Illustrator CC 22.0.1 to prepare figures

For manuscripts utilizing custom algorithms or software that are central to the paper but not yet described in the published literature, software must be made available to editors and reviewers upon request. We strongly encourage code deposition in a community repository (e.g. GitHub). *Nature Methods* guidance for providing algorithms and software for publication provides further information on this topic.

Materials and reagents

Policy information about availability of materials

8. Materials availability

Indicate whether there are restrictions on availability of unique materials or if these materials are only available for distribution by a for-profit company.	no restriction

9. Antibodies

Describe the antibodies used and how they were validated for use in the system under study (i.e. assay and species).	No antibodies were used

10. Eukaryotic cell lines

a. State the source of each eukaryotic cell line used.	no eukaryotic cell lines were used
b. Describe the method of cell line authentication used.	no eukaryotic cell lines were used
c. Report whether the cell lines were tested for mycoplasma contamination.	no eukaryotic cell lines were used
d. If any of the cell lines used are listed in the database of commonly misidentified cell lines maintained by ICLAC, provide a scientific rationale for their use.	no eukaryotic cell lines were used

Animals and human research participants

Policy information about studies involving animals; when reporting animal research, follow the ARRIVE guidelines

11. Description of research animals

Provide details on animals and/or animal-derived materials used in the study.	no animals were used in the study.

Policy information about studies involving human research participants

12. Description of human research participants

Describe the covariate-relevant population characteristics of the human research participants.	This study did not involve human research participants.